



# The impacts of thermal neutron scattering effect and resonance elastic scattering effect on FHRs



Zhifeng Li, Liangzhi Cao\*, Hongchun Wu, Qingming He

School of Nuclear Science and Technology, Xi'an Jiaotong University, Xi'an, Shaanxi 710049, China

## ARTICLE INFO

### Article history:

Received 26 February 2016  
Received in revised form 13 June 2016  
Accepted 7 July 2016  
Available online 15 July 2016

### Keywords:

TSL  
2LiF-BeF<sub>2</sub>  
Resonance elastic scattering  
DBRC  
FHRs

## ABSTRACT

Two effects in Fluoride-salt-cooled High-temperature Reactors (FHRs) are analyzed based on Monte Carlo simulation. Firstly, the thermal neutron scattering effect of fluoride salt (2LiF-BeF<sub>2</sub>) is considered by utilization of the newly generated Thermal neutron Scattering Library (TSL) files. It is found that the neutron spectrum becomes harder and the fission reaction rate of <sup>235</sup>U decreases at thermal energy range due to the up-scattering introduced by thermal neutron scattering effect. Secondly, the resonance elastic scattering effect of heavy nuclides in epithermal energy range is covered by implementation of the Doppler Broadening Rejection Correction (DBRC) method in MCNP. It is shown that neutron up-scattering is enhanced in the low energy wing of the resonance peak and neutron down-scattering is increased in the high energy wing of the resonance peak. This phenomenon leads to an increase in the neutron capture rate of <sup>238</sup>U by about 1.0%. For the analyzed FHR pebble unit cells at 1200 K depending on TRISO packing factor, the thermal neutron scattering effect of 2LiF-BeF<sub>2</sub> and the resonance elastic scattering effect result in a decrease in  $k_{inf}$  of 93–290 pcm and 131–591 pcm, respectively. By taking into account the two effects simultaneously, the  $k_{inf}$  of FHR pebble unit cells decreases by 248–881 pcm.

© 2016 Elsevier Ltd. All rights reserved.

## 1. Introduction

Monte Carlo codes usually adopt three strategies to deal with neutron scattering on target nuclides (Coveyou et al., 1956): (1) in thermal energy range (up to a few eV), chemical binding effect as well as the target motion is taken into account with the use of the  $S(\alpha, \beta)$  table. The  $S(\alpha, \beta)$  table is provided in the evaluated nuclear data files in the form of interpolation table for various alpha and beta which are calculated from incident neutron energies, scattered neutron energies and scattering angles. For nuclides lacking the  $S(\alpha, \beta)$  tables, the free gas scattering treatment is used for thermal energy ranges where the target nuclides are assumed to be unbound; (2) in the lower epithermal energy range, the chemical binding effect of material is negligible and the thermal motion of the target nuclides is described by the free gas elastic scattering model; (3) Above the threshold for free gas scattering, target-at-rest kinematics is used for higher epithermal neutron energy ranges and fast neutron (Zoja et al., 2013).

However, these strategies face some challenges when applied to the simulation of Fluoride-salt-cooled High-temperature Reactors (FHRs) (Zweibaum et al., 2014), which adopt fluoride salt coolant

and high temperature coated-particle fuel as two basic techniques. These challenges come from two aspects as follows.

Firstly, in the thermal energy range, the scattering is affected by the binding of the scattering nuclei in the solid or liquid moderator materials, and the neutron can give up energy to excitations in the material, or it can gain energy, it is the so-called 'thermal neutron scattering effect'. For the thermal neutron scattering effect changes the reaction cross section, modifies the energy and alters the energy and angle distribution of the scattered neutrons, so the thermal scattering library (TSL) of the traditional moderator materials such as H<sub>2</sub>O, D<sub>2</sub>O and graphite are available in the evaluated thermal neutron scattering sub-libraries (MacFarlane, 1994), however, TSL of the 2LiF-BeF<sub>2</sub> used in the FHRs is not available in existing ENDF/B format evaluated libraries, moreover lacking of the TSL of fluoride salt leads to overestimate the  $k_{eff}$  about 820 pcm for the Molten Salt Reactor Experiment (MSRE) (Mei et al., 2013), but no study focuses on the impact of thermal neutron scattering effect of the 2LiF-BeF<sub>2</sub> on the FHRs. Therefore it's necessary to process the TSL of the 2LiF-BeF<sub>2</sub> to quantify the thermal neutron scattering effect for the FHRs. In this paper, the LEAPR module of NJOY (MacFarlane and Muir, 1994) is adopted to generate TSL data of 2LiF-BeF<sub>2</sub>, and subsequently the ACE-format libraries of the 2LiF-BeF<sub>2</sub> are generated by NJOY to be provided to the MCNP code for quantification of the thermal neutron scattering effect of 2LiF-BeF<sub>2</sub>.

\* Corresponding author.

E-mail address: [caolz@mail.xjtu.edu.cn](mailto:caolz@mail.xjtu.edu.cn) (L. Cao).

Secondly, the resonance elastic scattering effect is not considered in epithermal energy range. Conventionally, the original free gas scattering kernel is adopted to take into account the thermal motion of the target. However, the original free gas scattering kernel ignores the energy-dependent scattering cross section in the sampling procedure of target velocity, therefore the original free gas scattering kernel it can't offer the precise differential scattering kernel for heavy nuclides (Sunny, 2013). In fact, when the neutron energy is in the vicinity of the elastic scattering resonance peaks within the epithermal energy range, the thermal motion of the target nuclei would significantly impacts the elastic scattering reaction rate and leads to augment of neutron capture, which is named the 'resonance elastic scattering effect' (Lee et al., 2008, 2009). Therefore, the new  $S(\alpha, \beta)$  scattering law tables (Dagan, 2005), the Doppler Broadening Rejection Correction (DBRC) method (Rothenstein, 1996; Becker et al., 2009a) and the Weight Correction Method (WCM) (Mori and Nagaya, 2009) are proposed to overcome the limitations of the original free gas scattering kernel. The DBRC method (Rothenstein, 1996; Becker et al., 2009a) is selected in this work over other methods to account for resonance elastic scattering effect because it is based on the free gas scattering kernel on which MCNP currently operates. The DBRC method considers the effects of energy-dependent cross sections via an additional rejection test, and it has been implemented and validated in MC21 (Sutton et al., 2007), TRIPOLI (Tripoli-4 Project Team, 2008; Zoia et al., 2013), MCNP (X-5 Monte Carlo Team, 2008; Sunny et al., 2012) and OpenMC (Romano and Forget, 2013; Walsh et al., 2014). The influence of the updated scattering kernel on high-temperature reactors, such as HTR and HTTR, was shown to be significant (Becker et al., 2009b). Similar to HTR and HTTR, the FHRs also work at high temperatures. Therefore it is necessary to take into account the resonance elastic scattering effect of heavy nuclei in FHRs. In this work, the resonance elastic scattering effect of FHRs is analyzed by Monte Carlo simulation with improved elastic scattering kernel introduced by DBRC method.

Based on the analysis mentioned above, the thermal neutron scattering effect of the 2LiF-BeF<sub>2</sub> mainly affects scattering reaction rate in thermal energy range and the resonance elastic scattering effect affects elastic scattering reaction rate in epithermal energy range, which would not interfere each other and it is necessary to take into account both of the two effects.

This work is organized in the following manner: the theory of the thermal neutron scattering, the schemes of generating the ENDF/B format TSL data of 2LiF-BeF<sub>2</sub> and the analysis of thermal neutron scattering are described in Section 2. The theory of the elastic scattering kernel and the validation of the implementation of the DBRC method in the MCNP are described in Section 3. In Section 4, the thermal neutron scattering effect of 2LiF-BeF<sub>2</sub> and resonance elastic scattering effect of heavy nuclei of FHRs are quantified. Finally conclusion remarks are given in Section 5.

## 2. Thermal neutron scattering of fluoride salt

### 2.1. Relevant theories of the thermal neutron scattering

The thermal neutron scattering cross section is usually divided into three different categories:

- (1) Inelastic scattering cross section. It is important for all materials, therefore it's important for both liquid 2LiF-BeF<sub>2</sub> molten salt (usually above 774 K) and solid 2LiF-BeF<sub>2</sub> crystals.
- (2) Coherent elastic cross section. It is important for crystalline solids like graphite, LiF and BeF<sub>2</sub> etc. Coherent elastic cross sections of solid 2LiF-BeF<sub>2</sub> crystals are also given in this work in case of fluoride salt is below 774 K.

- (3) Incoherent elastic cross section. It is important for hydrogenous solids such as light water ice, polyethylene and zirconium hydride.

The thermal neutron scattering cross section can be expressed as:

$$\sigma(E \rightarrow E', \mu) = \frac{\sigma_b}{2k_B T} \sqrt{\frac{E}{E'}} S(\alpha, \beta) \quad (1)$$

$$\alpha = \frac{E' + E - 2\mu\sqrt{EE'}}{Ak_B T} \quad (2)$$

$$\beta = \frac{E' - E}{k_B T} \quad (3)$$

where  $\alpha$  and  $\beta$  are the momentum transfer and the energy transfer respectively,  $E'$  is the scattered neutron energy,  $E$  is the incident neutron energy,  $\sigma_b$  is the characteristic bound scattering cross section for material,  $\mu$  is the cosine of scattering angle (in the lab system),  $A$  is the mass ratio of the scatterer to neutron and  $k_B T$  is the thermal energy in eV.

#### 2.1.1. Solid 2LiF-BeF<sub>2</sub> crystals

The solid-type scattering function is written as:

$$S_s(\alpha, \beta) = \frac{1}{2\pi} \int_{-\infty}^{\infty} e^{i\beta t} e^{-\gamma(t)} dt \quad (4)$$

$$\gamma(t) = \alpha \int_{-\infty}^{\infty} P_s(\beta) [1 - e^{-i\beta t}] \times e^{-\beta^2/2} d\beta \quad (5)$$

$$P_s(\beta) = \frac{\rho_s(\beta)}{2\beta \sinh(\beta/2)} \quad (6)$$

where  $S_s(\alpha, \beta)$  is the solid-type scattering function,  $\rho_s(\beta)$  is the frequency spectrum of excitations in the system and it is calculated by the CASTEP module of Material Studio (Refson, 2004) in this work (see Fig. 1). In 2LiF-BeF<sub>2</sub> crystal, the atom is the real particle of lattice vibration, but its quantum of collective vibration is described by phonon. The different phonon frequency corresponds to different fundamental mode of vibration, the phonon frequency spectrum is helpful to describe the vibration of 2LiF-BeF<sub>2</sub>.  $\gamma(t)$  is the Gaussian function for solid-type frequency spectra. The function  $P_s(\beta)$  defined by Eq. (6) is used directly in LEAPR module of NJOY code. Utilizing the phonon expansion, the scattering function defined by Eq. (4) becomes

$$S_s(\alpha, \beta) = e^{-\alpha\beta} \sum_{n=0}^{\infty} \frac{1}{n!} \alpha^n \times \frac{1}{2\pi} \int_{-\infty}^{\infty} e^{i\beta t} \left[ \int_{-\infty}^{\infty} P_s(\beta') e^{-\beta'^2/2} e^{-i\beta' t} d\beta' \right]^n dt \quad (7)$$

For large values of  $\alpha$ , the expansion of Eq. (7) requires extensive number of terms. Using the simple Short-Collision-Time (SCT) approximation from ENDF, the solid-type scattering law can be extended:

$$S_s(\alpha, \beta) = \frac{1}{\sqrt{4\pi\omega_s\alpha\bar{T}_s/T}} \exp\left[-\frac{(\omega_s\alpha - \beta)^2}{\omega_s\alpha\bar{T}_s/T}\right] \quad (8)$$

where  $\omega_s$  is the weight for the solid-type spectrum and the effective temperature  $\bar{T}_s$  is defined by:

$$\bar{T}_s = \frac{T}{2\omega_s} \int_{-\infty}^{\infty} \beta^2 P_s(\beta) e^{-\beta^2} d\beta \quad (9)$$

In solids consisting of coherent scatterers – for example, graphite, LiF and BeF<sub>2</sub> – the zero-phonon term leads to interference

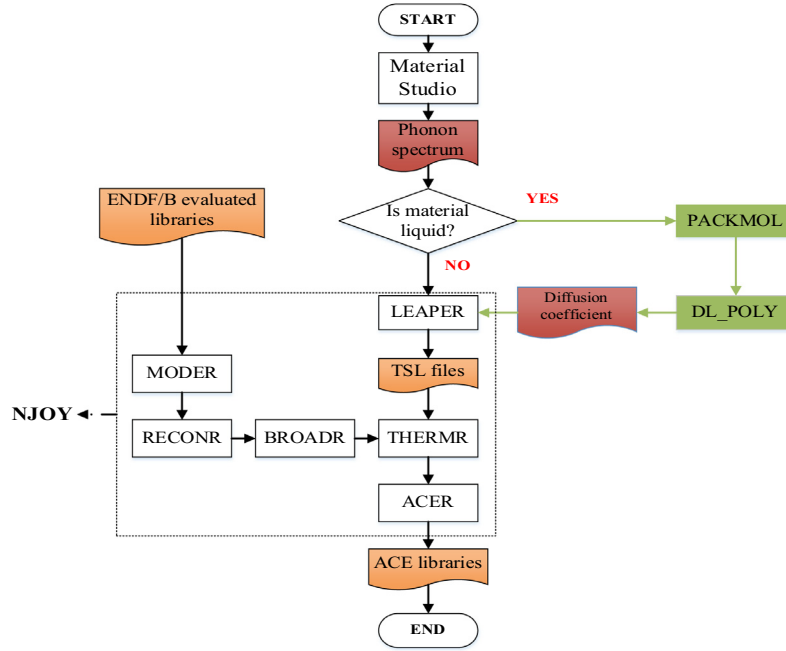


**Fig. 1.** Scheme of processing thermal neutron scattering data of solid 2LiF-BeF<sub>2</sub> and liquid 2LiF-BeF<sub>2</sub>. The black dotted line frame represents modules of NJOY code. The olive dashed part (PACKMOL + DL\_POLY) corresponds to the additional procedure for liquid fluoride salt.

scattering from atoms at various planes in lattices that making up the crystal. The coherent elastic scattering has no energy loss, and the scattering cross section of the coherent elastic scattering is given by

$$\sigma_{coh}(E, \mu) = \frac{\sigma_c}{E} \sum_{E_i < E} f_i e^{-4WE_i} \delta(\mu - \mu_i) \quad (10)$$

where

$$\mu_i = 1 - E_i/E \quad (11)$$

and the integrated cross section is given by

$$\sigma_{coh} = \frac{\sigma_c}{E} \sum_{E_i < E} f_i e^{-4WE_i} \quad (12)$$

where  $\sigma_c$  is the effective bound coherent scattering cross section,  $W$  is the effective Debye-Waller coefficient,  $E_i$  are the Bragg Edges,  $f_i$  are related to the crystallographic structure factors of the material.

### 2.1.2. Liquid 2LiF-BeF<sub>2</sub> molten salt

The thermal neutron scattering for liquid 2LiF-BeF<sub>2</sub> can be represented by combining a solid-type spectrum of rotational and vibrational modes  $S_s(\alpha, \beta)$  with a diffusion term  $S_t(\alpha, \beta)$ :

$$S(\alpha, \beta) = S_t(\alpha, \beta) e^{-\alpha^2} + \int_{-\infty}^{\infty} S_t(\alpha, \beta') S_s(\alpha, \beta - \beta') d\beta' \quad (13)$$

Egelstaff and Schofield (1962) proposed an effective width model for the diffusion term

$$S_t(\alpha, \beta) = \frac{2c\omega_t\alpha}{\pi} \exp[2c^2\omega_t\alpha - \beta/2] \times \frac{\sqrt{c^2 + 0.25}}{\sqrt{\beta^2 + 4c^2\omega_t^2\alpha^2}} K_1(\sqrt{c^2 + 0.25}\sqrt{\beta^2 + 4c^2\omega_t^2\alpha^2}) \quad (14)$$

and the associated frequency spectrum:

$$\rho_t(\beta) = \omega_t \frac{4c}{\pi\beta} \sqrt{c^2 + 0.25} \sinh(\beta/2) K_1(\sqrt{c^2 + 0.25}\beta) \quad (15)$$

where  $K_1(x)$  is a modified Bessel function of the second kind, and both the translational weight  $\omega_t$  and the diffusion constant  $c$  are input data for LEAPER. The translational weight  $\omega_t$  is given by:

$$\omega_t = 1/M \quad (16)$$

where  $M = 99$  is the effective mass of liquid 2LiF-BeF<sub>2</sub>. Because no discrete oscillator exist in liquid 2LiF-BeF<sub>2</sub>, the sum of  $\omega_t$  and  $\omega_s$  equals 1. Diffusion constants  $c$  of F, Li and Be are calculated by the molecular dynamics simulations code DL\_POLY (Smith et al., 2002), as shown in Fig. 1.

### 2.2. Scheme of generating thermal neutron scattering data

Based on the theories above, the thermal neutron scattering of the 2LiF-BeF<sub>2</sub> within FHRs is divided into two categories:

- (1) Inelastic scattering and coherent elastic scattering for solid 2LiF-BeF<sub>2</sub> crystals;
- (2) Inelastic scattering for liquid 2LiF-BeF<sub>2</sub> molten salt.

The generation of the thermal neutron scattering data for the 2LiF-BeF<sub>2</sub> is as shown in Fig. 1. According to Eq. (6), a phonon spectrum is required to calculate the thermal scattering law. A module of Material Studio named CASTEP (Refson, 2004) is used to generate the phonon spectrum for 2LiF-BeF<sub>2</sub>. The LEAPER, MODER, RECONR, BROADR, THERMR, ACER are modules of NJOY. The LEAPER module produces the thermal scattering data in ENDF-6 format which can be subsequently processed by the THERMR module, the THERMR module produces cross sections and energy-to-energy matrices for free or bound scatterers in the thermal energy range.

Compared with the solid 2LiF-BeF<sub>2</sub> crystals, both the phonon spectrum and diffusion coefficient are required to calculate the  $S_t(\alpha, \beta)$  of Eq. (14) for liquid 2LiF-BeF<sub>2</sub> molten salt. The phonon spectrum has been calculated by the Material Studio. Molecular dynamics simulations of liquid fluoride salt are performed by the DL\_POLY software package to calculate the diffusion coefficients of F, Li and Be. The auxiliary PACKMOL software (Martinez et al.,

2009) is used to obtain the initial configuration of each composition by placing the appropriate number of atoms randomly without any overlap.

### 2.3. Analysis of the thermal neutron scattering cross section

According to the processing scheme in Fig. 1, the phonon frequency spectrum of 2LiF-BeF<sub>2</sub> is shown in Fig. 2. It is found that the acoustic modes are contributed by heavier F atoms while the optic modes are contributed by lighter Be and Li atoms.

#### 2.3.1. Inelastic and coherent elastic scattering for solid 2LiF-BeF<sub>2</sub>

Thermal neutron scattering cross section of solid 2LiF-BeF<sub>2</sub> contains inelastic scattering cross section and coherent elastic scattering cross section. Scattering cross sections of BeF<sub>2</sub> and LiF at 300 K, 600 K are shown in Figs. 3 and 4. As observed from these two figures, the inelastic cross section curve is smooth. However, the elastic cross section curve is complicated. As shown in Figs. a and b, the coherent elastic cross section defined by Eq. (12) is zero below the first Bragg edge  $E_1$ . Then the coherent elastic cross section jumps sharply to a value determined by  $f_1$  and the Debye-Waller term. At higher energy region, the cross section drops off as  $1/E$  until  $E = E_2$ . It then takes another jump and resumes its  $1/E$  drop-off. The sizes of the steps in the cross section gradually become smaller. At high energy region, the steps attenuate and the cross section shows an asymptotic  $1/E$  decreasing trend. Furthermore, the inelastic cross section at 600 K is greater than that at 300 K in low energy range of the thermal energy

range, but the elastic cross section at 300 K is greater than that at 600 K in high energy range of the thermal energy range. Moreover, the thermal scattering cross section of Be bound in BeF<sub>2</sub> generated by this work and Be bound in Be metal, Be bound in BeO of ENDFB-VII.1 are compared, as shown in Fig. 5. It is found that despite the similar trend, significant difference exists in both inelastic scattering cross sections and elastic scattering cross sections.

#### 2.3.2. Inelastic scattering for liquid 2LiF-BeF<sub>2</sub>

Different from solid materials, there only exists inelastic scattering cross section within liquid materials (Squires, 1978). In order to carry out the following neutron-physics calculations, inelastic scattering cross section of F bound-atom, Li bound-atom and Be bound-atom at 900 K, 1000 K and 1200 K are processed in this work and shown in Figs. 6–8. It can be found that the scattering cross sections of F bound-atom, Li bound-atom and Be bound-atom decrease with the temperature. Fig. 9 shows that secondary neutron energy spectrum of F bound-atom, Li bound-atom and Be bound-atom at 1200 K, in general, the average scattering neutron energy is bigger than the incident neutron energy which means that the up-scattering is significant in 2LiF-BeF<sub>2</sub>.

In addition, the inelastic cross sections of 2LiF-BeF<sub>2</sub> at 1175 K generated by this work are compared with that of the literature (Mei et al., 2013), it shows a good agreement between them in Fig. 10, which illustrates the thermal neutron scattering cross section of 2LiF-BeF<sub>2</sub> is correctly processed.

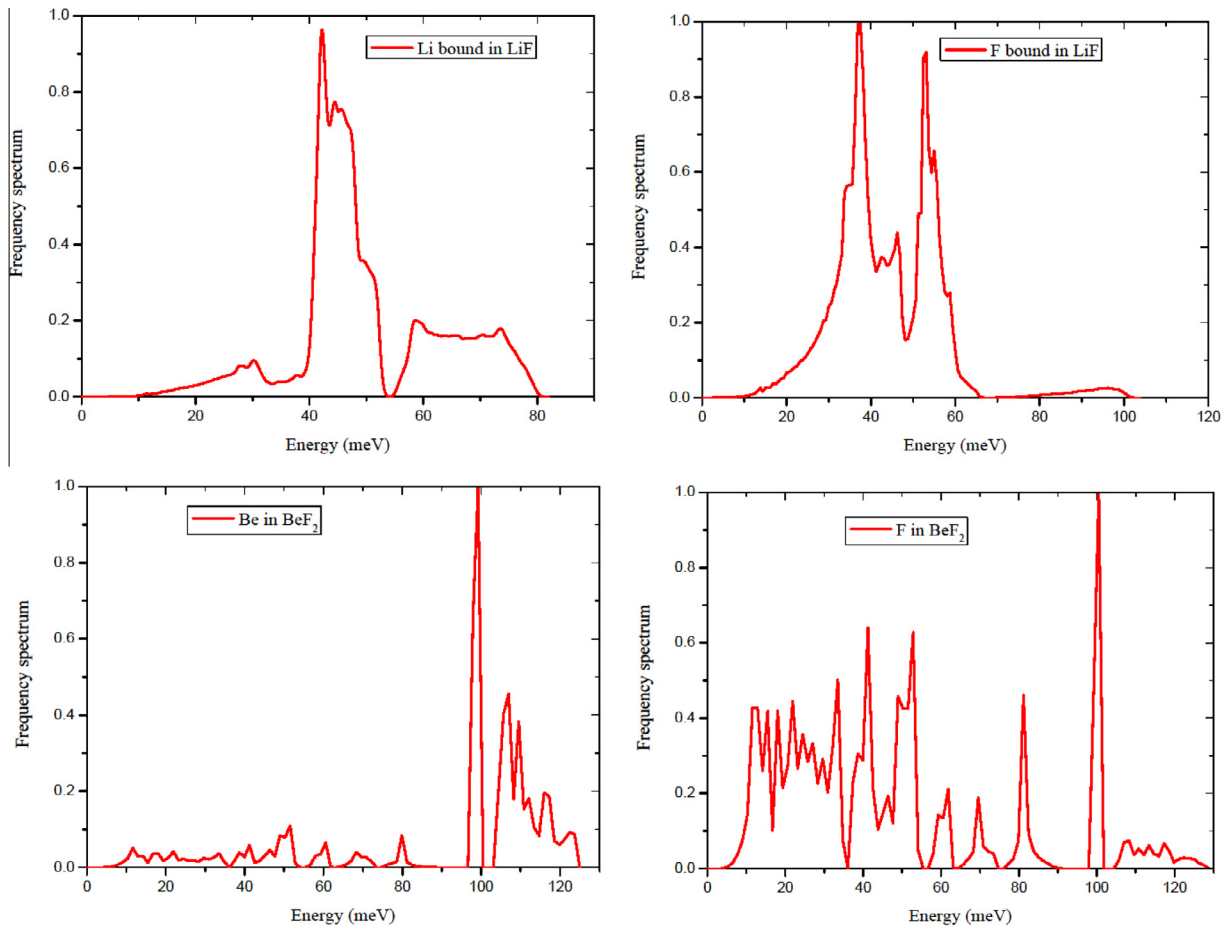


Fig. 2. Phonon frequency spectrum of the 2LiF-BeF<sub>2</sub>.

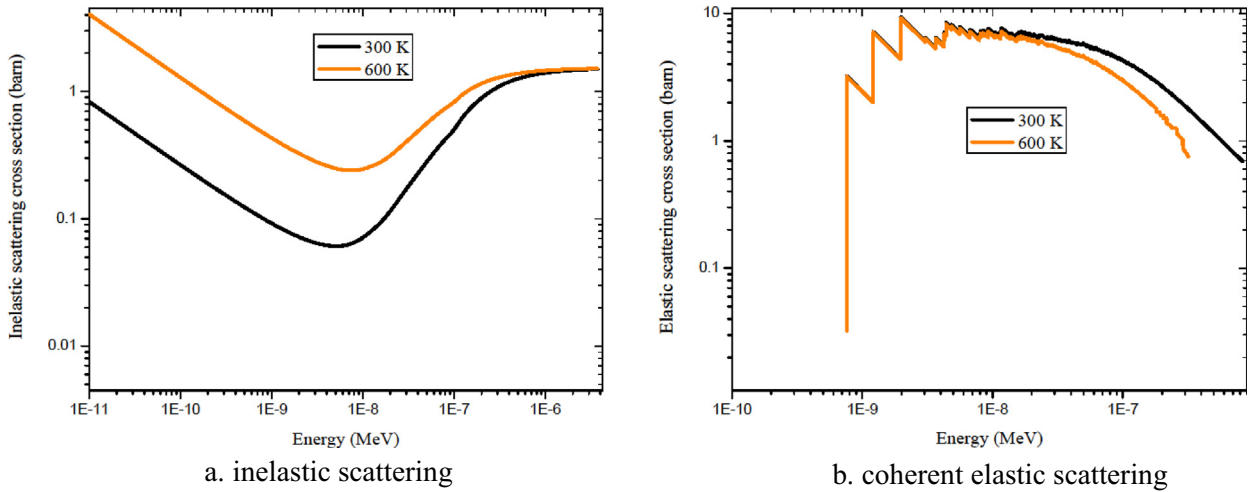


Fig. 3. Inelastic scattering cross section and coherent elastic scattering cross section of BeF<sub>2</sub> at 300 K and 600 K.

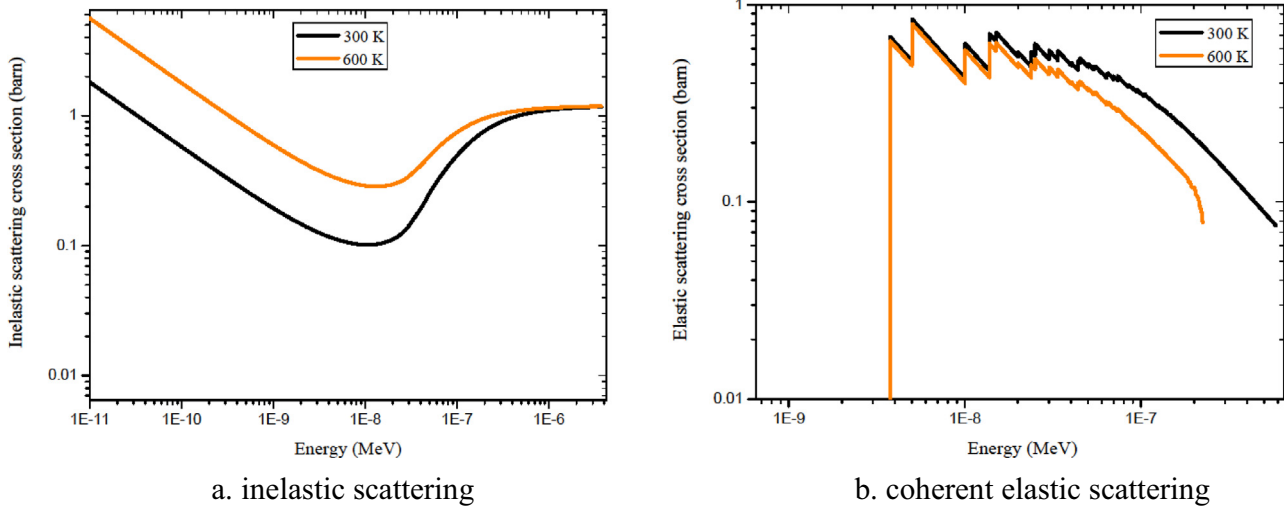


Fig. 4. Inelastic scattering cross section and coherent elastic scattering cross section of LiF at 300 K and 600 K.

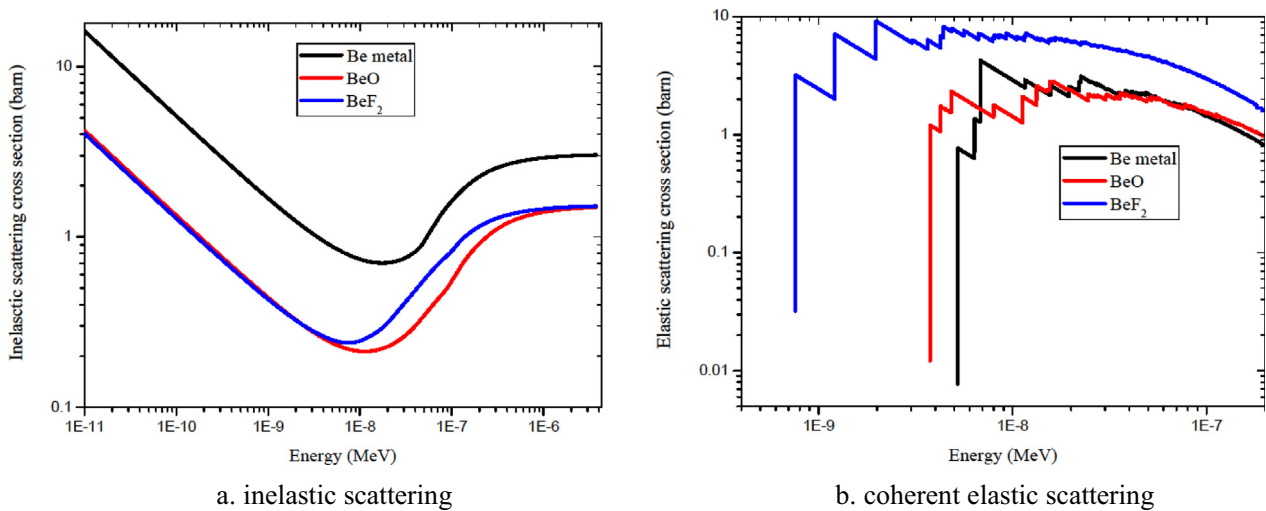


Fig. 5. Difference of the scattering cross section of Be bound in Be metal, BeO and BeF<sub>2</sub> at 600 K.

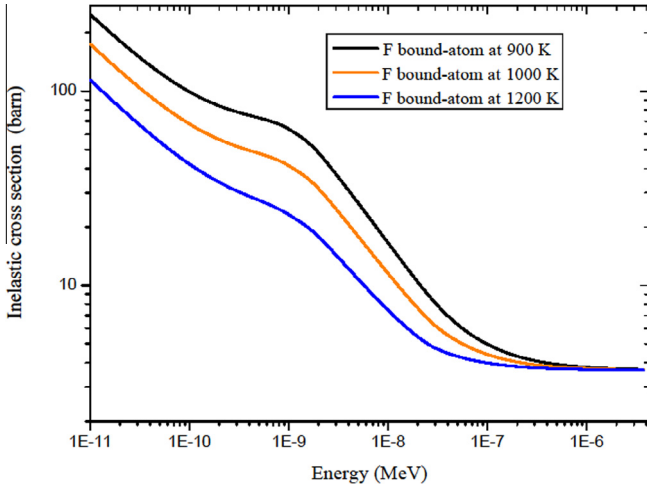


Fig. 6. The inelastic scattering cross section of F bound-atom at 900 K, 1000 K and 1200 K.

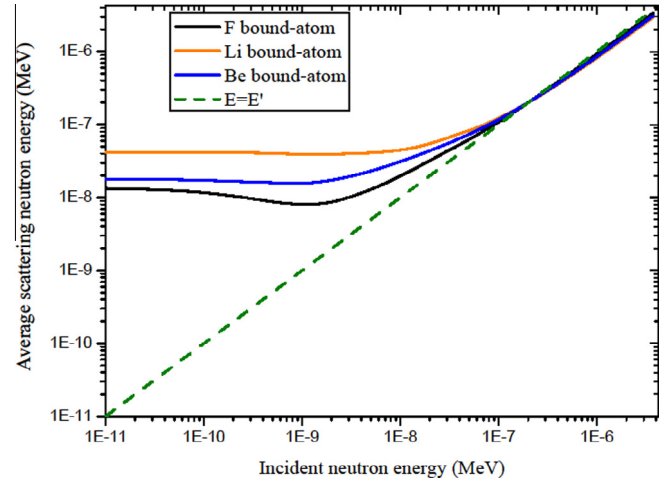


Fig. 9. The secondary neutron energy spectrum of F, Li and Be at 1200 K compared with  $E = E'$  (the olive dash line,  $E$  is incident neutron energy,  $E'$  is the average scattering neutron energy).

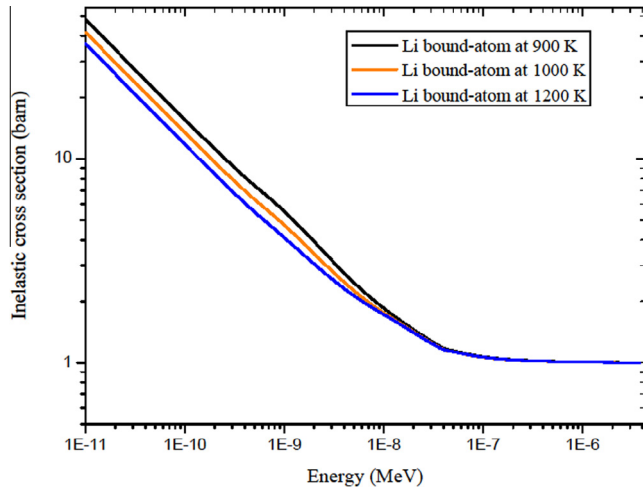


Fig. 7. The inelastic scattering cross section of Li bound-atom at 900 K, 1000 K and 1200 K.

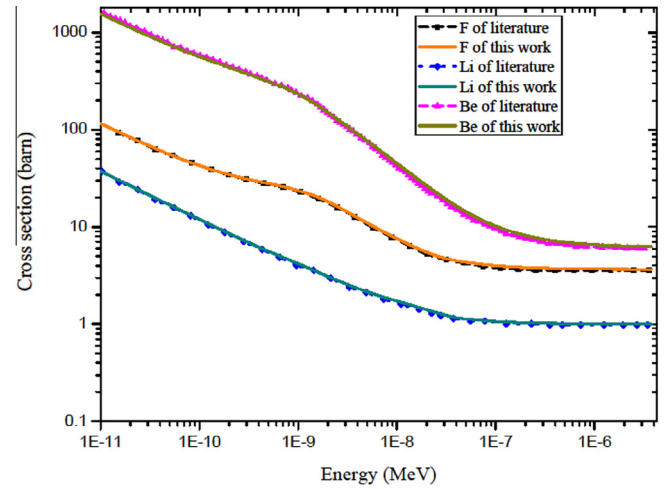


Fig. 10. The validation of inelastic scattering cross section of F, Li and Be at 1175 K.

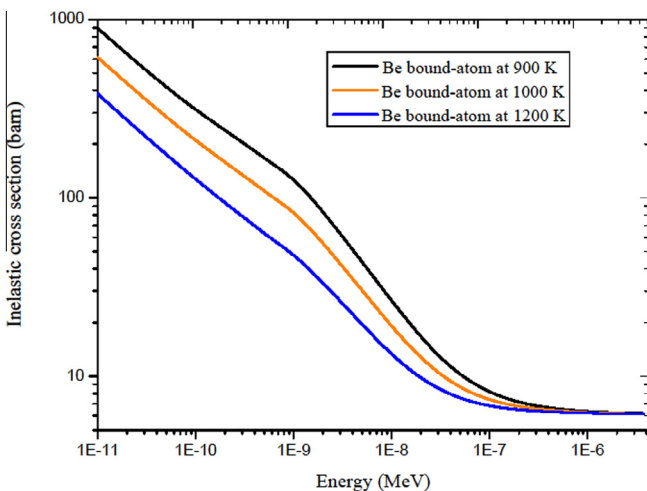


Fig. 8. The inelastic scattering cross section of Be bound-atom at 900 K, 1000 K and 1200 K.

### 3. The resonance elastic scattering for epithermal neutrons

#### 3.1. Implement of the DBRC method

The original free gas scattering kernel assumes that the elastic scattering cross section of the target at 0 K changes negligibly over the range of the relative speed between neutron and target, namely, the energy-dependent scattering cross section is ignored in the sampling procedure of target velocity. But when the target nucleus is resonance nuclei such as  $^{238}\text{U}$ , the basic assumption is not valid. Therefore the DBRC method (Becker et al., 2009a) is proposed to account for the energy-dependent elastic scattering cross section and the thermal motion of target. The improved target probability density function is:

$$P(V, \mu|v_N) = B \left\{ \frac{\sigma_S(v_R, 0)}{\sigma_S^{\text{MAX}}(v_\xi, 0)} \right\} \left\{ \frac{v_R}{V + v_N} \right\} \{P_1 f_1(V) + P_2 f_2(V)\} \quad (17)$$

$$B = \frac{(\sqrt{\pi}\beta v_N + 2)\sigma_S^{\text{MAX}}(v_R, 0)}{2\sqrt{\pi}\beta v_N \sigma_S^{\text{eff}}(v_N, T)} \quad (18)$$

$$v_{\xi} \in \left[ v_N - \frac{4}{\sqrt{\alpha}}, v_N + \frac{4}{\sqrt{\alpha}} \right] \quad (19)$$

$$\alpha = \frac{M_t}{2k_B T} \quad (20)$$

where  $V$  is the speed of the target,  $v_R$  is the relative speed between incident neutron and target nucleus,  $v_N$  is the speed of incident neutron,  $M_t$  is the mass of target,  $v_{\xi}$  is a dimensionless speed,  $\sigma_{MAX} S(v_{\xi}, 0)$  is the maximum value of elastic scattering cross sections within a range of the dimensionless speed determined by Eq. (19), the  $V$  is sampled from  $f_1(V)$  with probability  $P_1$  and from  $f_2(V)$  with probability  $P_2$ , the  $\mu$  is uniformly sampled from  $[-1, 1]$ . The  $v_R/(V + v_N)$  and  $\sigma_S(v_R, 0)/\sigma_{MAX} S(v_{\xi}, 0)$  are the first and second rejection test applied to the sampled velocity of the target. The modified scattering kernel model based on DBRC method is implemented in MCNP to accurately evaluate the resonance scattering in the energy range [0.4, 210] eV.

### 3.2. Comparison of the double-differential scattering kernels

Figs. 11 and 12 show the comparison of the original free gas (FG) scattering kernel and the DBRC kernels of  $^{238}\text{U}$  at 1200 K with neutron incident energy to be 6.52 eV and 6.9 eV, respectively. In the vicinity of the resonance peaks, there are significant differences between FG and DBRC. Compared with the original FG model, enhanced neutron up-scattering can be observed when the DBRC method is applied. As shown in Fig. 10, when the incident neutron energy (6.52 eV) is lower than the resonance peak (6.76 eV), the up-scattering is enhanced. In contrast, as shown in Fig. 12, when the incident neutron energy (6.90 eV) is higher than the resonance peak (6.76 eV), more neutrons are down-scattered into the resonance peak from the right wing of the resonance peak. The enhanced up-scattering phenomenon is widely observed by other researchers (Sunny et al., 2012; Zoia et al., 2013; Trumbull and Fieno, 2013). The down-scattering phenomenon observed in this work is consistent with that observed by other researchers (Walsh et al., 2014). The more neutrons are scattered towards the resonance peak, the more neutrons will be captured by  $^{238}\text{U}$ .

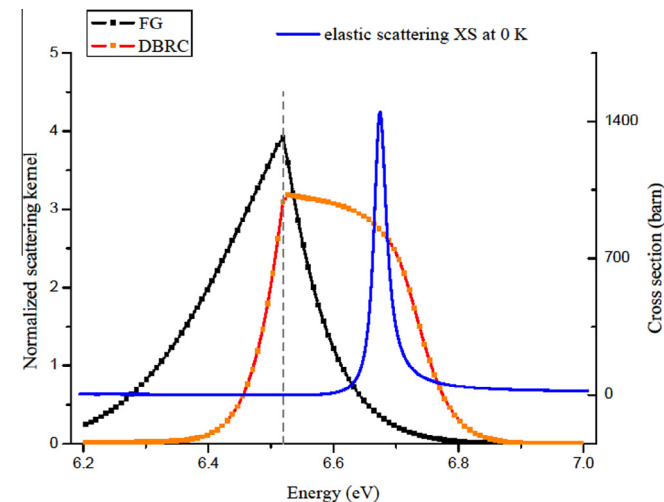


**Fig. 11.** Comparison of normalized elastic scattering kernels using FG and DBRC on  $^{238}\text{U}$  with incident energy at 6.52 eV at 1200 K. Black curve is standard MCNP calculation using FG; red curve is improved MCNP calculation using DBRC. Grey dashed line represents source neutron emitting at 6.52 eV. The right second level diagram (the blue curve) represents the elastic scattering cross section at 0 K, which is used in the DBRC sampling loop. (For interpretation of the references to colour in this figure legend, the reader is referred to the web version of this article.)

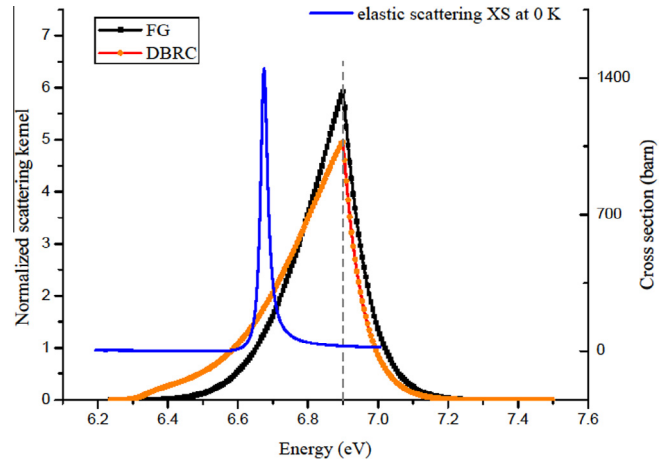


**Fig. 12.** Comparison of normalized elastic scattering kernels using FG and DBRC on  $^{238}\text{U}$  with incident energy at 6.90 eV at 1200 K. Black curve is standard MCNP calculation using FG; red curve is improved MCNP calculation using DBRC. Grey dashed line represents source neutron emitting at 6.90 eV. (For interpretation of the references to colour in this figure legend, the reader is referred to the web version of this article.)

This trend will be enhanced with the increasing temperature (see Figs. 13 and 14).

### 3.3. The verification of DBRC method

The Mosteller Doppler reactivity defect benchmark (Mosteller, 2006) is adopted to verify the DBRC method implemented in this work. The eigenvalue calculations of  $\text{UO}_2$  pin cell at Hot Zero Power (HZP) and Hot Full Power (HFP) are carried out by both standard MCNP and improved MCNP. The eigenvalues obtained by applying standard MCNP with FG and improved MCNP with DBRC are summarized in Tables 1 and 2. The impact of resonance elastic scattering on  $k_{inf}$  for  $\text{UOX}$  fuel problems at HZP and HFP are given in Tables 3 and 4. The impact of resonance elastic scattering on  $k_{inf}$  for  $\text{MOX}$  pin cell at HZP and HFP are given in Table 5. The eigenvalue differences computed by the FG scattering kernel and resonance elastic scattering kernel are also compared with the results of other codes, such as TRIPOLI-4 based on WCM method and DBRC method (Zoia et al., 2013), MVP-2 (Nagaya et al., 2005) based on WCM method (Mori and Nagaya, 2009) and MCNP5 based on DBRC

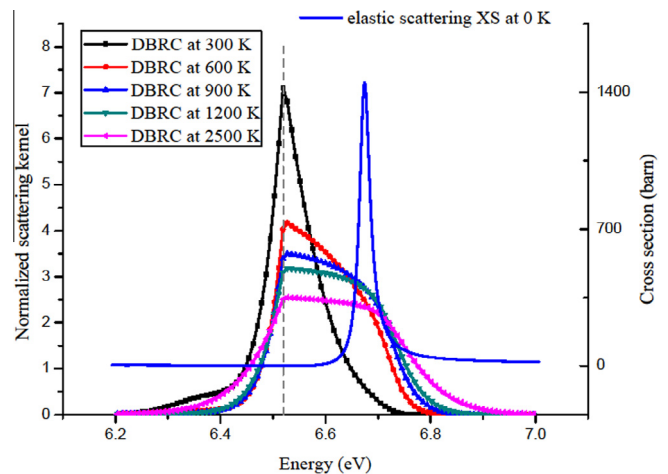


**Fig. 13.** Comparison of normalized elastic scattering kernels using DBRC on  $^{238}\text{U}$  with incident energy at 6.52 eV at different temperatures. Grey dashed line represents source neutron emitting at 6.52 eV.

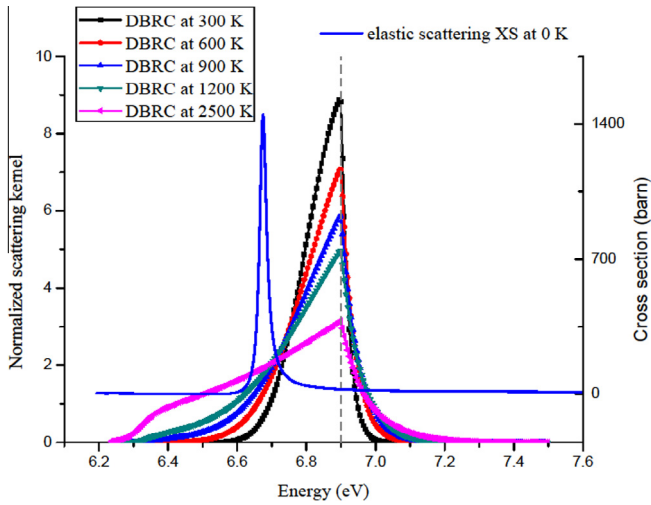


**Fig. 14.** Comparison of normalized elastic scattering kernels using DBRC on <sup>238</sup>U with incident energy at 6.90 eV at different temperatures. Grey dashed line represents source neutron emitting at 6.90 eV.

method (Sunny et al., 2012). As observed in these tables, the DBRC method brings out a deviation of the  $k_{inf}$  from 47 pcm to 76 pcm at HZP and 130 pcm to 165 pcm at HFP with the uranium enrichments ranging from 0.711% to 5.0% in UOX fuel. For the MOX fuel, with the plutonium content ranging from 1% to 8%, the DBRC method achieves a deviation of the  $k_{inf}$  from 54 pcm to 126 pcm at HZP and 151 pcm to 217 pcm at HFP. The conclusion of Tables 3–5 can be drawn that despite small discrepancies, these results

obtained in this work are generally consistent with those of other researchers. Furthermore, the calculation results of this work are generally better than that of the previous MCNP calculations. The possible cause of observed calculation discrepancies between them is the different calculation conditions. Compared with results obtained by other researchers, the exact scattering kernel based on DBRC method which is implemented in MCNP can evaluate the resonance scattering effect accurately. Therefore the improved MCNP code can be applied to evaluate the resonance scattering effect of the FHRs.

**4. The impacts of the thermal neutron scattering and the resonance elastic scattering effect on FHRs**

The impacts of the thermal neutron scattering effect within coolant and resonance elastic scattering effect within fuel are investigated with regard to FHRs pebble cells. The detailed specifications of the coated particle, pebble and coolant are given in Table 6.

The TRISO geometric design of pebble unit cell is the same as that of the HTR-10 (IAEA, 2003) and each layer of TRISO is simulated exactly. The TRISO particles are embedded in the matrix. The TRISO packing factor (TPF) is defined as the volume fraction of the TRISO particles in the matrix. Reflective boundary conditions are used. The FHRs pebble unit cell modeled by MCNP is shown in Fig. 15.

**4.1. The impact of thermal neutron scattering on pebble unit cell**

The temperatures of all the nuclides except 2LiF-BeF<sub>2</sub> are kept constant at 1000 K. The eigenvalue calculation results of the pebble

**Table 1**  
Mostellers benchmark. The  $k_{inf}$  ( $1\sigma$ ) values for UOX fuel with uranium enrichments ranging from 0.711% to 5.0%. Calculations are performed using MCNP with FG and DBRC.

wt. (%)	HZP-FG	HZP-DBRC	HFP-FG	HFP-DBRC
0.711	0.66558 (0.00006)	0.66527 (0.00006)	0.65981 (0.00006)	0.65885 (0.00006)
1.6	0.96086 (0.00009)	0.96013 (0.00009)	0.95257 (0.00008)	0.95118 (0.00009)
2.4	1.09907 (0.00010)	1.09823 (0.00010)	1.08982 (0.00010)	1.08827 (0.00010)
3.1	1.17685 (0.00009)	1.17621 (0.00011)	1.16757 (0.00010)	1.16564 (0.00010)
3.9	1.23966 (0.00010)	1.23880 (0.00010)	1.22981 (0.00010)	1.22798 (0.00011)
4.5	1.27530 (0.00010)	1.27437 (0.00010)	1.26492 (0.00010)	1.26327 (0.00010)
5.0	1.29943 (0.00011)	1.29878 (0.00010)	1.28929 (0.00010)	1.28727 (0.00011)

**Table 2**  
Mosteller benchmark. The  $k_{inf}$  ( $1\sigma$ ) values for MOX fuel with plutonium content ranging from 1% to 8%. Calculations are performed using MCNP with FG and DBRC.

wt. (%)	HZP-FG	HZP-DBRC	HFP-FG	HFP-DBRC
1	0.94500 (0.00010)	0.94381 (0.00010)	0.93540 (0.00010)	0.93337 (0.00010)
2	1.02077 (0.00011)	1.01949 (0.00010)	1.00960 (0.00011)	1.00762 (0.00010)
4	1.07559 (0.00011)	1.07474 (0.00011)	1.06389 (0.00011)	1.06189 (0.00011)
6	1.10413 (0.00012)	1.10348 (0.00011)	1.09259 (0.00011)	1.09062 (0.00011)
8	1.12768 (0.00011)	1.12707 (0.00011)	1.11607 (0.00011)	1.11439 (0.00011)

**Table 3**  
Influence of resonance elastic scattering on  $k_{inf}$  for UOX at HZP ( $\frac{k_{DBRC}-k_{FG}}{k_{FG}} \times 10^5$ , unit : pcm).

wt. (%)	TRIPOLI-DBRC	TRIPOLI-WCM	MVP-WCM	MCNP5-DBRC	MCNP-DBRC (This work)
0.711	-99	-115	-101	-9	-47
1.6	-117	-135		-74	-76
2.4	-100	-127	-91	-35	-76
3.1	-98	-107		-62	-54
3.9	-82	-110	-106	-70	-69
4.5	-78	-95		-38	-73
5.0	-88	-106	-82	-89	-50

**Table 4**  
Influence of resonance elastic scattering on  $k_{inf}$  for UOX at HFP ( $\frac{k_{res}-k_{ref}}{k_{ref}} \times 10^5$ , unit : pcm).

wt. (%)	TRIPOLI-DBRC	TRIPOLI-WCM	MVP-WCM	MCNP5-DBRC	MCNP-DBRC(This work)
0.711	-186	-227	-180	-86	-145
1.6	-171	-225		-191	-146
2.4	-206	-220	-205	-150	-142
3.1	-174	-204		-133	-165
3.9	-178	-179	-182	-114	-149
4.5	-175	-216		-153	-130
5.0	-174	-189	-182	-119	-157

**Table 5**  
Influence of resonance elastic scattering on  $k_{inf}$  for MOX at HZP and HFP ( $\frac{k_{res}-k_{ref}}{k_{ref}} \times 10^5$ , unit : pcm).

wt. (%)	TRIPOLI-DBRC (HZP)	MCNP-DBRC (HZP)	TRIPOLI-DBRC (HFP)	MCNP-DBRC (HFP)
1	-118	-126	-229	-217
2	-122	-125	-218	-196
4	-109	-79	-205	-188
6	-98	-59	-181	-180
8	-95	-54	-183	-151

**Table 6**  
Parameters of pebble unit cell.

Item	Value
<i>Fuel pebble specification</i>	
Diameter of ball/cm	6.0
Diameter of fueled zone/cm	5.0
Density of graphite in fueled zone and outer shell/g/cm <sup>3</sup>	1.73
Enrichment of <sup>235</sup> U/%	16.82
Natural boron impurities in uranium/ppm	4
Natural boron impurities in graphite/ppm	1.3
Volumetric filling fraction of balls in core/%	0.6046
<i>Coated particle specification</i>	
Radius of fuel kernel/cm	0.025
UO <sub>2</sub> density with kernel/g/cm <sup>3</sup>	10.4
Coating layer material(starting from kernel)	PyC/PyC/SiC/PyC
Coating layer thickness/cm	0.009/0.004/0.0035/0.004
Coating layer density/g/cm <sup>3</sup>	1.1/1.9/3.18/1.9
<i>Coolant specification</i>	
Material	2LiF-BeF <sub>2</sub> (0.005% <sup>6</sup> Li)

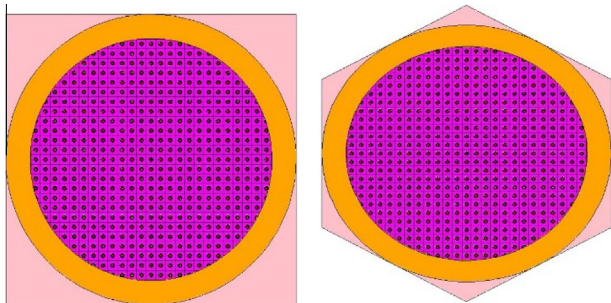


**Fig. 15.** Vertical and horizontal view of the FHR pebble unit cell.

unit cell for different TPF and coolant temperatures are presented in Table 7. Each calculation is performed twice: the first one is done by standard MCNP with only the thermal neutron scattering cross section library of graphite. The first calculation results are referred to as the ‘Reference’. The second calculation is done by standard MCNP with the thermal neutron scattering cross section

**Table 7**  
Infinite multiplication factor  $k_{inf}$  ( $1\sigma$ ) of pebble unit cell for different TPF and coolant temperatures.

TPF/pebble	5.0%	7.5%	10%	15%	30%
Reference (case 1)	1.48030 (0.00010)	1.48279 (0.00011)	1.45851 (0.00011)	1.39661 (0.00012)	1.25405 (0.00012)
TSL (case 1)	1.47938 (0.00010)	1.48061 (0.00011)	1.45585 (0.00011)	1.39356 (0.00012)	1.25091 (0.00012)
Reference (case 2)	1.48011 (0.00010)	1.48205 (0.00011)	1.45732 (0.00011)	1.39543 (0.00012)	1.25362 (0.00012)
TSL (case 2)	1.47886 (0.00010)	1.48020 (0.00011)	1.45513 (0.00011)	1.39286 (0.00012)	1.25067 (0.00012)
Reference (case 3)	1.48003 (0.00010)	1.48123 (0.00011)	1.45688 (0.00011)	1.39456 (0.00012)	1.25277 (0.00012)
TSL (case 3)	1.47821 (0.00010)	1.47900 (0.00011)	1.45407 (0.00011)	1.39146 (0.00012)	1.24908 (0.00012)
Reference (case 4)	1.47979 (0.00010)	1.48116 (0.00011)	1.45638 (0.00011)	1.39447 (0.00012)	1.25262 (0.00012)
TSL (case 4)	1.47834 (0.00010)	1.47916 (0.00011)	1.45385 (0.00011)	1.39145 (0.00012)	1.24870 (0.00012)
Reference (case 5)	1.47947 (0.00010)	1.48053 (0.00011)	1.45598 (0.00011)	1.39373 (0.00012)	1.25204 (0.00012)
TSL (case 5)	1.47794 (0.00010)	1.47885 (0.00011)	1.45335 (0.00011)	1.39097 (0.00012)	1.24851 (0.00012)

Case 1: 2LiF-BeF<sub>2</sub> at 300 K; case 2: 2LiF-BeF<sub>2</sub> at 600 K; case 3: 2LiF-BeF<sub>2</sub> at 900 K; case 4: 2LiF-BeF<sub>2</sub> at 1000 K; case 5: 2LiF-BeF<sub>2</sub> at 1200 K.

**Table 8**  
The relative infinite multiplication factor differences ( $\frac{k_{TSL}-k_{reference}}{k_{reference}} \times 10^5$ ) of pebble unit cell for different TPF and temperatures.

TPF/pebble	5.0%	7.5%	10%	15%	30%
Case 1	-62	-142	-182	-218	-250
Case 2	-84	-125	-150	-184	-235
Case 3	-123	-150	-193	-222	-295
Case 4	-98	-135	-174	-217	-313
Case 5	-103	-113	-181	-198	-282

Case 1: 2LiF-BeF<sub>2</sub> at 300 K; case 2: 2LiF-BeF<sub>2</sub> at 600 K; case 3: 2LiF-BeF<sub>2</sub> at 900 K; case 4: 2LiF-BeF<sub>2</sub> at 1000 K; case 5: 2LiF-BeF<sub>2</sub> at 1200 K.

library of both fluoride salt and graphite. The second calculation results are identified by ‘TSL’ in Table 7. The ‘TSL’ results are smaller than ‘Reference’ results due to the addition of the TSL of fluoride salt. Moreover, the absolute difference increases with the increase in TPF in Table 8. For the case of 2LiF-BeF<sub>2</sub> at 300 K, 600 K, 900 K, 1000 K and 1200 K, the absolute difference introduced by the thermal neutron scattering effect increases 62–250 pcm, 84–235 pcm, 123–295 pcm, 98–313 pcm and 103–282 pcm with the increasing TPF, respectively.

#### 4.2. The impact of resonance elastic scattering on pebble unit cell

The pebble unit adopted in this section is the same as in section 4.1, the only difference is that the temperatures of all nuclides except UO<sub>2</sub> are kept constant at 1000 K. The eigenvalue calculations of the pebble unit cell for different TPF and UO<sub>2</sub> temperatures

**Table 9**

Infinite multiplication factor  $k_{inf}$  ( $1\sigma$ ) of pebble unit cell for different TPF and fuel temperatures.

TPF/pebble	5.0%	7.5%	10%	15%	30%
Reference (case 1)	1.48342 (0.00010)	1.48639 (0.00011)	1.46251 (0.00011)	1.40190 (0.0012)	1.26143 (0.00012)
DBRC (case 1)	1.48219 (0.00010)	1.48424 (0.00011)	1.45997 (0.00012)	1.39851 (0.00012)	1.25653 (0.00012)
Reference (case 2)	1.47300 (0.00010)	1.47209 (0.00011)	1.44541 (0.00011)	1.38063 (0.00012)	1.23670 (0.00012)
DBRC (case 2)	1.47101 (0.00010)	1.46919 (0.00011)	1.44163 (0.00012)	1.37555 (0.00012)	1.22940 (0.00012)
Reference (case 3)	1.44450 (0.00011)	1.43201 (0.00011)	1.39639 (0.00012)	1.31963 (0.00012)	1.16349 (0.00012)
DBRC (case 3)	1.44054 (0.00010)	1.42619 (0.00012)	1.38940 (0.00012)	1.30994 (0.00012)	1.14974 (0.00012)

Case 1:  $UO_2$  at 900 K; case 2:  $UO_2$  at 1200 K; case 3:  $UO_2$  at 2500 K.

are presented in Table 9. Each calculation is performed twice: the first one is performed by the standard MCNP using FG, the second one is performed with the improved MCNP using DBRC. Both calculations are without thermal neutron scattering library of  $2LiF-BeF_2$ . The first calculation results is as ‘Reference’ values, the second calculation results are identified by ‘DBRC’ in Table 10. All the eigenvalue calculation results of improved MCNP with DBRC method are smaller than results of standard MCNP with FG model. Moreover, the difference ascends with the increasing TPF and temperature in Table 10. Take the case of TPF = 30% for example, the absolute difference introduced by the elastic resonance scattering effect increases 388–1182 pcm with the increasing temperature. And for the case of  $UO_2$  at 2500 K, the absolute difference introduced by the elastic resonance scattering effect increases 274–1182 pcm with the increasing TPF.

4.3. The total impact of thermal neutron scattering and resonance elastic scattering effect on pebble unit cell

4.3.1. Eigenvalues of pebble unit cell

The pebble unit adopted in this section is the same as above. The only difference is that the temperatures of the all nuclides are kept constant at 1200 K. Each calculation is performed four times: the first calculation is performed by the standard MCNP without thermal neutron scattering library of  $2LiF-BeF_2$ , the second one is performed with the standard MCNP with the thermal neutron scattering library of  $2LiF-BeF_2$ , the third one is performed by the improved MCNP version without thermal neutron scattering library of  $2LiF-BeF_2$  and the last one is performed by the improved MCNP with the thermal neutron scattering library of  $2LiF-BeF_2$ . The first calculation results are the reference values, the second ones are identified by ‘TSL’, the third ones are identified by ‘DBRC’ and the last are identified by ‘TSL + DBRC’ in Table 11. The eigenvalues calculation results of ‘TSL’ and ‘DBRC’ are smaller than results of the reference ones. The differences introduce by ‘TSL’, ‘DBRC’ and ‘TSL + DBRC’ are also given in Table 11. The differences enlarge with the increase in TPF. The thermal neutron scattering effect introduced by adding TSL of  $2LiF-BeF_2$  and the resonance elastic

**Table 10**

The relative infinite multiplication factor differences ( $\frac{k_{DBRC}-k_{reference}}{k_{reference}} \times 10^5$ ) of pebble unit cell for different TPF and temperatures.

TPF/pebble	5.0%	7.5%	10%	15%	30%
Case 1	-123	-145	-174	-339	-388
Case 2	-135	-197	-262	-368	-590
Case 3	-274	-406	-500	-734	-1182

Case 1:  $UO_2$  at 900 K; case 2:  $UO_2$  at 1200 K; case 3:  $UO_2$  at 2500 K.

**Table 11**

Infinite multiplication factor and its relative difference of pebble unit cell for different TPF at 1200 K.

TPF/pebble	5.0%	7.5%	10%	15%	30%
$k_{inf}$ ( $1\sigma$ )					
Reference	1.46952 (0.00010)	1.46884 (0.00011)	1.44255 (0.00011)	1.37832 (0.00012)	1.23539 (0.00012)
TSL	1.46816 (0.00010)	1.46663 (0.00011)	1.44024 (0.00011)	1.37548 (0.00012)	1.23181 (0.00012)
DBRC	1.46759 (0.00010)	1.46585 (0.00011)	1.43852 (0.00011)	1.37334 (0.00012)	1.22809 (0.00012)
TSL + DBRC	1.46587 (0.00010)	1.46378 (0.00011)	1.43604 (0.00011)	1.37053 (0.00012)	1.22451 (0.00012)
Relative difference: $\frac{k_x - k_{reference}}{k_{reference}} \times 10^5$ ; unit: pcm					
Reference					
TSL	-93	-150	-160	-206	-290
DBRC	-131	-204	-279	-361	-591
TSL + DBRC	-248	-344	-451	-565	-881

scattering effect introduced by using DBRC lead to a decrease in  $k_{inf}$  of 93–290 pcm and 131–591 pcm, respectively. By taking into account the two effects together, the  $k_{inf}$  of FHR pebble unit cells decrease by 248–881 pcm. Namely, the difference introduced by ‘TSL + DBRC’ is approximately equal to the sum of differences introduced by ‘TSL’ and ‘DBRC’. The thermal neutron scattering effect and resonance elastic scattering effect of FHR are negative effects for  $k_{inf}$  and does not interfere each other.

4.3.2. Neutron spectrum and reaction rate of pebble unit cell

The impact of thermal neutron scattering effect on neutron spectrum is shown in Fig. 16a. The thermal neutron scattering effect hardens the spectrum at thermal energy range. Namely, the flux for lower thermal energy range decrease (see Fig. 16b) and the flux for higher thermal energy range neutrons increase (see Fig. 16c, and 5 eV is the maximum energy for thermal treatment). It can be explained by the up-scattering introduced by the thermal neutron scattering effect of  $2LiF-BeF_2$ . The impact of the thermal neutron scattering effect on the absolute fission reaction rate of  $^{235}U$  is studied and the differences at 1200 K are shown in Fig. 17. The reaction rate is estimated based on 7 energy group with the group boundaries to be: (1)  $48.30-1 \times 10^7$  (eV); (2) 27.60–48.30 (eV); (3) 15.90–27.60 (eV); (4) 9.91–15.90 (eV); (5) 5.04–9.91 (eV); (6) 0.22–5.04 (eV); (7)  $1 \times 10^{-5}$ –0.22 (eV). The neutron fission of  $^{235}U$  markedly decreases at energy group seven

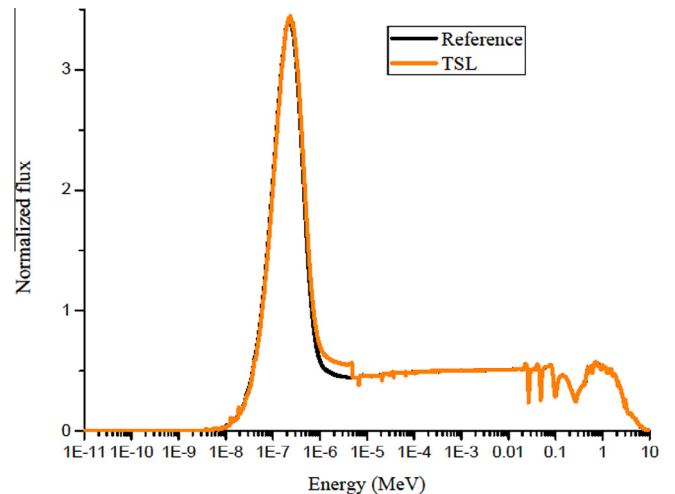


Fig. 16a. The impact of thermal neutron scattering effect to spectrum at total energy range [ $1 \times 10^{-5}$ ,  $1 \times 10^7$ ] (eV) for TPF = 5.0%, T = 1200 K.

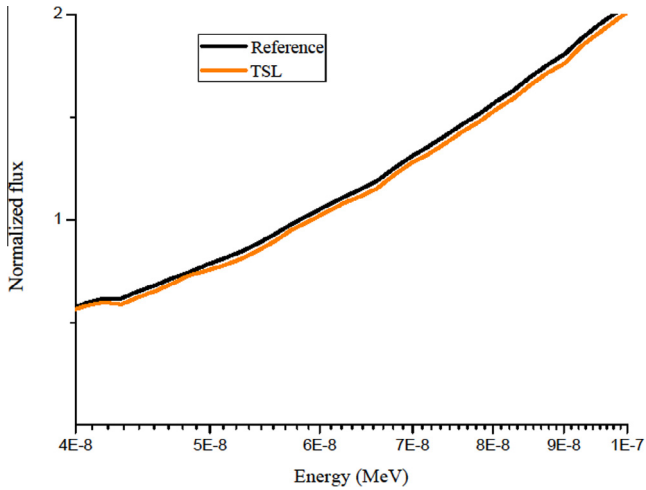


Fig. 16b. The impact of thermal neutron scattering effect to spectrum at energy range [0.004, 0.1] (eV) for TPF = 5.0%, T = 1200 K.

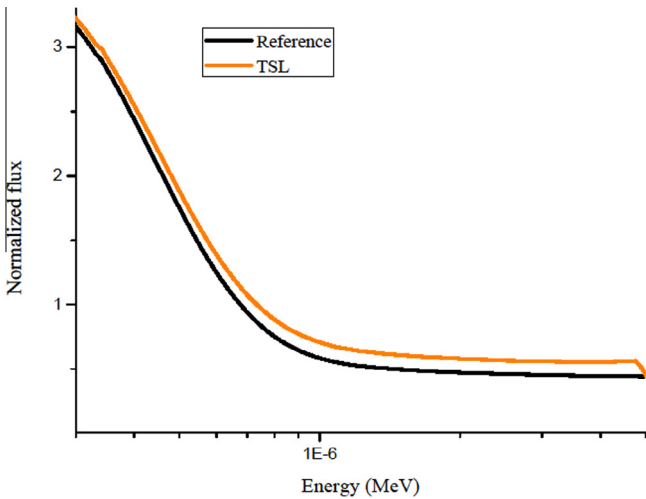


Fig. 16c. The impact of thermal neutron scattering effect to spectrum at energy range [0.3, 5] (eV) for TPF = 5.0%, T = 1200 K.

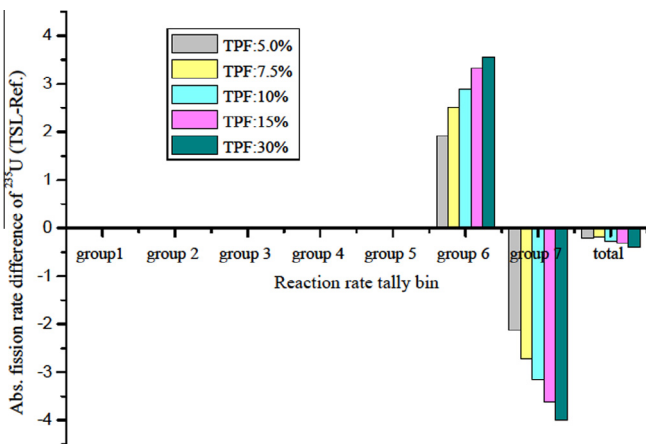


Fig. 17. The absolute fission reaction rate difference of the <sup>235</sup>U by ‘TSL – Reference’ for different TPF at 1200 K. Seven energy groups and the total energy region are used: (group1) 48.30–1 × 10<sup>7</sup> (eV); (group2) 27.60–48.30 (eV); (group3) 15.90–27.60 (eV); (group4) 9.91 – 15.90 (eV); (group5) 5.04–9.91 (eV); (group6) 0.22–5.04 (eV); (group7) 1 × 10<sup>-5</sup>–0.22 (eV); (8) total energy region: 1 × 10<sup>-5</sup>–1 × 10<sup>7</sup> (eV).

and significantly increases at energy group six due to the enhanced up-scattering taking place in the energy range of 0–5 eV. The total absolute fission reaction rate of <sup>235</sup>U decreases due to the thermal neutron scattering effect of the 2LiF-BeF<sub>2</sub>. Moreover the total absolute fission reaction rate differences of <sup>235</sup>U approximately enlarge with the increasing TPF.

The absorption reaction rate differences of the 2LiF-BeF<sub>2</sub> by ‘TSL – Reference’ for different TPF at 1200 K are shown in Fig. 18. The hardened thermal energy range spectrum results in a decrease absorption of the 2LiF-BeF<sub>2</sub> at group seven and an increase absorption of the 2LiF-BeF<sub>2</sub> at group six, respectively. They counteract each other nearly, only a tiny change of the absorption reaction rate is observed in the total energy range, therefore the thermal neutron scattering of 2LiF-BeF<sub>2</sub> mainly impacts the fission reaction of <sup>235</sup>U. Especially, the total absorption reaction rate difference of 2LiF-BeF<sub>2</sub> is less than zero when TPF = 5.0%, which would weaken the negative effect introduced by the decrease of the fission reaction rate of <sup>235</sup>U. Based on an overall consideration of fission reaction rate of <sup>235</sup>U the absorption reaction rate of the 2LiF-BeF<sub>2</sub>, it can explain the fact that the difference of *k<sub>inf</sub>* introduced by ‘TSL’ augments with the increasing TPF (see Tables 8 and 11).

Even though both <sup>235</sup>U and <sup>238</sup>U have pronounced resonance structure, however the neutron reaction rates of <sup>235</sup>U are dominated by its fission process, <sup>238</sup>U is expected to be the most important nuclei impacted by the DBRC correction, therefore only the capture reaction rate of <sup>238</sup>U is given in this work. The difference of the capture reaction rate of <sup>238</sup>U of ‘DBRC’ and ‘Reference’ for different TPF at 1200 K are shown in Fig. 19. It is necessary to note that the first three main resonance peaks of <sup>238</sup>U at 6.67 eV, 20.87 eV and 36.7 eV are in energy group five, three and two, respectively. Neutrons captured by <sup>238</sup>U at energy group five, three and two increase obviously due to the enhanced resonance elastic scattering effect of the DBRC method. The absolute capture reaction rate differences of <sup>238</sup>U of ‘TSL’ and ‘DBRC’ in total energy range raise with the increasing TPF, and the relative capture reaction rate of <sup>238</sup>U in total energy range augments by 0.97%–1.33% with the increasing TPF at 1200 K. The increased neutron capture of <sup>238</sup>U leads to a decrease of the *k<sub>inf</sub>* of the pebble unit cell. In addition, the deviation of the DBRC resonance elastic scattering kernel and FG scattering kernel rises with the increasing temperature, that is, higher fuel temperature leads to a stronger up scattering and down scattering towards the resonance and therefore more

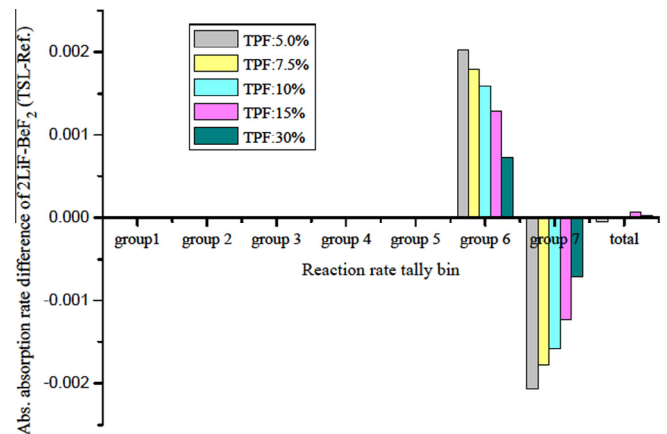
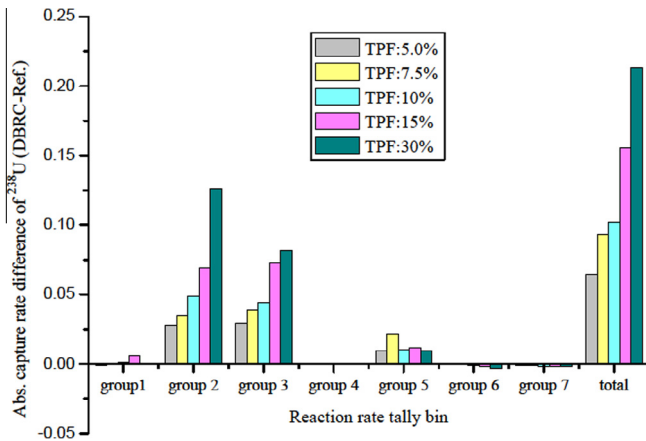


Fig. 18. The absolute absorption reaction rate differences of the 2LiF-BeF<sub>2</sub> by ‘TSL – Reference’ for different TPF at 1200 K. Seven energy groups and the total energy region are used: (group1) 48.30–1 × 10<sup>7</sup> (eV); (group2) 27.60–48.30 (eV); (group3) 15.90–27.60 (eV); (group4) 9.91 – 15.90 (eV); (group5) 5.04–9.91 (eV); (group6) 0.22–5.04 (eV); (group7) 1 × 10<sup>-5</sup>–0.22 (eV); (8) total energy region: 1 × 10<sup>-5</sup>–1 × 10<sup>7</sup> (eV).



**Fig. 19.** The absolute capture reaction rate difference of the  $^{238}\text{U}$  by ‘DBRC – Reference’ for different TPF at 1200 K. Seven energy groups and the total energy region are used: (group1)  $48.30\text{--}1 \times 10^7$  (eV); (group2) 27.60–48.30 (eV); (group3) 15.90–27.60 (eV); (group4) 9.91–15.90 (eV); (group5) 5.04–9.91 (eV); (group6) 0.22–5.04 (eV); (group7)  $1 \times 10^{-5}$ –0.22 (eV); (8) total energy region:  $1 \times 10^{-5}$ – $1 \times 10^7$  (eV).

neutrons are absorbed by  $^{238}\text{U}$ . Consequently, the difference of  $k_{inf}$  caused by resonance elastic scattering effect will augment with the increasing TPF and the temperature (see Table 10).

According to Figs. 17 and 18, the thermal neutron scattering effect has an impact on the energy group seven and six (namely, the energy range of [0, 5] eV). However, as shown in Fig. 19, the resonance elastic scattering effect has an impact on the energy group five, three and two (that is, the energy range of [5, 48] eV). Since the thermal neutron scattering effect impacts the thermal energy range while the resonance elastic scattering effect affects the epithermal energy range, the impacts of the two negative effects would not interfere each other, which can explain the fact that the  $k_{inf}$  differences introduced by ‘TSL + DBRC’ are practically equal to the sum of differences introduced by ‘TSL’ and ‘DBRC’ respectively.

## 5. Conclusion

The thermal neutron scattering library files of the  $2\text{LiF-BeF}_2$  are obtained by combining the phonon distribution calculation software Material Studio, the initial molecular configuration code PACKMOL, the molecular dynamics code DL\_POLY and modified nuclear data processing code NJOY for the exact treatment of thermal neutron scattering of the  $2\text{LiF-BeF}_2$ . The Doppler Broadening Rejection Correction (DBRC) method is supplemented and validated in MCNP for the exact treatment of resonance elastic scattering.

The thermal neutron scattering effect of the  $2\text{LiF-BeF}_2$  results in a decrease of fission reaction rate of  $^{235}\text{U}$  within thermal energy range, and the resonance elastic scattering effect brings about a significant increase of capture reaction rate of  $^{238}\text{U}$  within epithermal energy range. All the two effects lead to a decrease of the  $k_{inf}$  of the analyzed FHR pebble unit cells. Moreover the difference of  $k_{inf}$  caused by the thermal neutron scattering effect of the  $2\text{LiF-BeF}_2$  raises with the increasing TPF and the difference of  $k_{inf}$  caused by the resonance elastic scattering effect augments with the increasing TPF and temperature.

Both the two effects are negative effects for  $k_{inf}$ , moreover the thermal neutron scattering effects impacts the thermal energy range and the resonance elastic scattering effect influences the epithermal energy range, which indicates the two negative effects

would not interfere each other. It can explain the fact that the differences introduced by the two negative effects is approximately equal to the sum of differences introduced by the thermal neutron scattering effect and the resonance elastic scattering effect respectively. Take the analyzed FHR pebble unit cells at 1200 K for example, the thermal neutron scattering effect of  $2\text{LiF-BeF}_2$  and resonance elastic scattering effect lead to a decrease in  $k_{inf}$  of 93–290 pcm and 131–591 pcm respectively, and by taking into account the two effects together, the  $k_{inf}$  of FHR pebble unit cells decrease by 248–881 pcm. This work suggests that it’s necessary to take into consideration the thermal neutron scattering effect and resonance elastic scattering effect simultaneously during the conceptual design and engineering management of the FHRs.

## Acknowledgement

This work is financially supported by the National Natural Science Foundation of China (Grant No. 11522544).

## References

- Becker, B., Dagan, R., Lohnert, G., 2009a. Proof and implementation of the stochastic formula for ideal gas, energy dependent scattering kernel. *Ann. Nucl. Energy* 36, 470–474.
- Becker, B., Dagan, R., Broeders, C.H.M., 2009b. Improvement of the resonance scattering treatment in MCNP in view of HTR calculations. *Ann. Nucl. Energy* 36, 281–285.
- Coveyou, R.R., Bate, R.R., Osborn, R.K., 1956. Effect of moderator temperature upon neutron flux in infinite capturing medium. *J. Nucl. Energy* 2, 153–167.
- Dagan, R., 2005. On the use of  $S(\alpha, \beta)$  tables for nuclides with well pronounced resonances. *Ann. Nucl. Energy* 32, 367–377.
- Egelstaff, P.A., Schofield, P., 1962. On the evaluation of the thermal neutron scattering law. *Nucl. Sci. Eng.* 12, 260–270.
- IAEA, 2003. Evaluation of high temperature gas cooled reactor performance. Benchmark analysis related to initial testing of the HTTR and HTR-10. In: Nuclear Power Technology Development Section. International Atomic Energy Agency, p. 255. IAEA-TECDOC-1382.
- Lee, D., Smith, K., Rhodes, J., 2008. The impact of  $^{238}\text{U}$  resonance elastic scattering approximations on thermal reactor Doppler reactivity. In: PHYSOR 2008, Interlaken, Switzerland, September 14–19, 2008.
- Lee, D., Smith, K., Rhodes, J., 2009. The impact of  $^{238}\text{U}$  resonance elastic scattering approximations on thermal reactor Doppler reactivity. *Ann. Nucl. Energy* 36, 274–280.
- MacFarlane, R.E., 1994. New Thermal Neutron Scattering Files for ENDF/B-VI Release 2, LA-12639-MS. Los Alamos National Laboratory, Los Alamos, NM, USA.
- MacFarlane, R.E., Muir, D.W., 1994. The NJOY Nuclear Data Processing System, Version 91, Los Alamos National Laboratory Report LA-12740-M.
- Martinez, L., Andrade, R., Birgin, E.G., et al., 2009. PACKMOL: a package for building initial configurations for molecular dynamics simulations. *J. Comput. Chem* 30 (13), 2157–2164.
- Mei, L., Cai, X., Jiang, D., et al., 2013. The investigation of thermal neutron scattering data for molten salt FLiBe. *J. Sci. Technol.* 50 (7), 682–688.
- Mori, T., Nagaya, Y., 2009. Comparison of resonance elastic scattering models newly implemented in MVP continuous-energy Monte Carlo code. *J. Nucl. Sci. Technol.* 46, 793–798.
- Mosteller, R.D., 2006. Computational Benchmarks for the Doppler Reactivity Defect.
- Nagaya, Y., Okumura, K., Mori, T., Nakagawa, M., 2005. MVP/GMVP II: general purpose Monte Carlo codes for neutron and photon transport calculations based on continuous energy and multigroup methods, doi: JAERI 1348.
- Refson, K., 2004. CASTEP User Guide. CCLRC Rutherford Appleton Laboratory.
- Romano, P.K., Forget, B., 2013. The OpenMC Monte Carlo particle transport code. *Ann. Nucl. Energy* 51, 274–281.
- Rothenstein, W., 1996. Neutron scattering kernels in pronounced resonances for stochastic doppler effect calculations. *Ann. Nucl. Energy* 23, 441–458.
- Smith, W., Yong, C., Rodger, P., 2002. DL\_POLY: application to molecular simulation. *Mol. Simul.* 28 (5), 385–471.
- Squires, G.L., 1978. Introduction to the Theory of Thermal Neutron Scattering. Cambridge University Press, New York, p. 87.
- Sunny, E.E., 2013. On-The-Fly Generation of Differential Resonance Scattering Probability Distribution Functions for Monte Carlo Codes (A dissertation submitted in partial fulfillment of the requirements for the degree of Doctor of Philosophy). Nuclear Engineering and Radiological Sciences in the University of Michigan.
- Sunny, E.E., Brown, F.B., Kiedrowski, B.C., et al., 2012. Temperature effects of resonance scattering for epithermal neutrons in mcnp. In: PHYSOR 2012, Knoxville, Tennessee, USA, April 15–20, 2012, on CD-ROM, pp. 1–9.
- Sutton, T.M., Donovan, T.J., Trumbull, T.H., et al., 2007. The MC21 Monte Carlo code. In: Proc. Int. Conf. on Mathematics & Computations and Supercomputing in Nuc. Applications.

- Tripoli-4 Project Team, 2008. Tripoli-4 User Guide, CEA-R-6169. French Alternative Energies and Atomic Energy Commission.
- Trumbull, T.H., Fieno, T.E., 2013. Effects of applying the doppler broadened rejection correction method for LEU and MOX pin cell depletion calculations. *Ann. Nucl. Energy* 62, 184–194.
- Walsh, J.A., Forget, B., Smith, K.S., 2014. Accelerated sampling of the free gas resonance elastic scattering kernel. *Ann. Nucl. Energy* 69, 116–124.
- X-5 Monte Carlo Team, 2008. MCNP A General Monte Carlo N-Particle Transport Code, Version 5, LA-UR-03-1987. Los Alamos National Laboratory.
- Zoia, A., Brun, E., Jouanne, C., et al., 2013. Doppler broadening of neutron elastic scattering kernel in TRIPOLI-4. *Ann. Nucl. Energy* 54, 218–226.
- Zweibaum, N., Cao, G., Cisneros, A.T., et al., 2014. Phenomenology, methods and experimental program for fluoride-salt-cooled, high-temperature reactors (FHRs). *Prog. Nucl. Energy* 77, 390–405.